



**Cite this article:** Muraro D *et al.* 2018 Chronic TNF $\alpha$ -driven injury delays cell migration to villi in the intestinal epithelium. *J. R. Soc. Interface* **15**: 20180037.

<http://dx.doi.org/10.1098/rsif.2018.0037>

Received: 15 January 2018

Accepted: 3 July 2018

**Subject Category:**

Life Sciences – Mathematics interface

**Subject Areas:**

biomathematics, computational biology, systems biology

**Keywords:**

intestinal crypts, cell migration, cell-based model, compartmental model

**Author for correspondence:**

Daniele Muraro

e-mail: [daniele.muraro@sanger.ac.uk](mailto:daniele.muraro@sanger.ac.uk)

Electronic supplementary material is available online at <https://dx.doi.org/10.6084/m9.figshare.c.4159451>.

# Chronic TNF $\alpha$ -driven injury delays cell migration to villi in the intestinal epithelium

Daniele Muraro<sup>1,2</sup>, Aimee Parker<sup>3</sup>, Laura Vaux<sup>3</sup>, Sarah Filippi<sup>4,5</sup>, Axel A. Almet<sup>1</sup>, Alexander G. Fletcher<sup>6</sup>, Alastair J. M. Watson<sup>7</sup>, Carmen Pin<sup>3</sup>, Philip K. Maini<sup>1</sup> and Helen M. Byrne<sup>1</sup>

<sup>1</sup>Wolfson Centre for Mathematical Biology, Mathematical Institute, University of Oxford, Oxford, UK

<sup>2</sup>Wellcome Trust Sanger Institute, Wellcome Trust Genome Campus, Hinxton, Cambridgeshire, UK

<sup>3</sup>Gut Health and Food Safety Research Programme, Institute of Food Research, Norwich, UK

<sup>4</sup>Department of Mathematics, and <sup>5</sup>Department of Epidemiology and Biostatistics, Imperial College London, London, UK

<sup>6</sup>School of Mathematics and Statistics and Bateson Centre, University of Sheffield, Sheffield, UK

<sup>7</sup>Norwich Medical School, University of East Anglia, Norwich, UK

DM, 0000-0001-9601-237X; AGF, 0000-0003-0525-4336

The intestinal epithelium is a single layer of cells which provides the first line of defence of the intestinal mucosa to bacterial infection. Cohesion of this physical barrier is supported by renewal of epithelial stem cells, residing in invaginations called crypts, and by crypt cell migration onto protrusions called villi; dysregulation of such mechanisms may render the gut susceptible to chronic inflammation. The impact that excessive or misplaced epithelial cell death may have on villus cell migration is currently unknown. We integrated cell-tracking methods with computational models to determine how epithelial homeostasis is affected by acute and chronic TNF $\alpha$ -driven epithelial cell death. Parameter inference reveals that acute inflammatory cell death has a transient effect on epithelial cell dynamics, whereas cell death caused by chronic elevated TNF $\alpha$  causes a delay in the accumulation of labelled cells onto the villus compared to the control. Such a delay may be reproduced by using a cell-based model to simulate the dynamics of each cell in a crypt–villus geometry, showing that a prolonged increase in cell death slows the migration of cells from the crypt to the villus. This investigation highlights which injuries (acute or chronic) may be regenerated and which cause disruption of healthy epithelial homeostasis.

## 1. Introduction

The intestinal epithelium is a rapidly self-renewing tissue, formed of a single layer of cells, that covers the luminal surface of the small and large intestine, providing a barrier to bacterial infection. Epithelial cells in the small intestine are organized into numerous protrusions, termed villi and invaginations, termed crypts of Lieberkühn. Self-renewal is sustained by the proliferative activity of adult stem cells at the base of intestinal crypts whose progeny proliferate and then differentiate into the functionally distinct epithelial subtypes that migrate onto the villus where they are eventually shed into the gut lumen [1]. Such cellular dynamics can be thought of as a ‘conveyor belt’ where cell proliferation acts as the principal driving force for cell migration on villi [2]. Perturbations of this tightly controlled process may be responsible for the development of serious diseases. For example, excessive or misplaced cell death may disrupt barrier function and cause chronic inflammation; on the other hand, deficiency in cell death may lead to cancer development [3]. In combination with experimental studies, mathematical modelling helps us to disentangle the complex interactions underlying the self-renewal of the intestinal epithelium under healthy and pathological conditions. The cellular dynamics of

the intestinal epithelium have been studied using a variety of theoretical approaches, including compartmental models based on ordinary differential equations (ODEs) [4,5], continuum models [6] and cell-based models [7–17]. Experimental and theoretical studies of the influence of reduced or halted proliferation on epithelial homeostasis showed a pronounced coupling of cell proliferation with cell migration onto villi [2,18]. However, it remains unknown whether an increase in cell death in the epithelium affects villus cell migration and how excessive cell death on a particular villus influences epithelial homeostasis in neighbouring crypts.

Here, we use a multidisciplinary approach to determine how two types of induced enterocyte cell death affect cell migration on villi in two regions of the mouse small intestine (ileum and duodenum). Epithelial cell death was induced by exposure to  $\text{TNF}\alpha$ , a cytokine involved in systemic inflammation, for different time periods and levels.  $\text{TNF}\alpha$  is well documented as an initiating agent in mouse models of inflammatory bowel disease and has previously been used to study chronic inflammatory processes of the intestine [19–24]. However, we recognize that intestinal inflammation involves a multitude of cytokine and cellular responses, many of which may not be recapitulated in our  $\text{TNF}\alpha$ -only models, which may more strictly be described as  $\text{TNF}\alpha$ -driven models of increased epithelial cell death, or more simply acute and chronic ‘injury’. During ‘acute injury’, the mice expressed a high level of circulating  $\text{TNF}\alpha$  for around 90 min before levels returned to baseline; this treatment caused cleaved-Caspase-3 positive (apoptotic) cell death and detachment from villus tips. During ‘chronic injury’, the mice expressed a lower circulating level of  $\text{TNF}\alpha$  for two weeks continuously prior to and during the measurements; this treatment induced less severe, but more persistent, cell death.

To investigate epithelial cell dynamics during acute and chronic injury, we applied cell-tracking methods to monitor accumulation of labelled cells along the crypt–villus axis following exposure of healthy crypts to high and low doses of  $\text{TNF}\alpha$ . We generated experimental time courses from crypt–villus epithelial units indicating the number of cells that were tracked (labelled) in the crypt and villus compartments. A previous analysis of the kinetics of villus cell populations in mice involved deriving a median villus transit time [25]. Although this measurement may provide interesting information about the villus kinetics, the scope of our article is to quantify the contribution to migration in time from the crypt and to estimate how such contribution may be affected by cell death due to  $\text{TNF}\alpha$ . For this reason, we developed mathematical models describing the dynamics along the crypt–villus unit which couple the effects of cell proliferation, migration and death. Complementary information was derived from two different computational approaches, namely cell-based and compartmental models, as follows. We replicated the experiments, simulating injury in a cell-based model in which cells are confined to a two-dimensional surface comprising four crypts, adjacent to a villus, with cells moving according to a nearest-neighbour-defined repulsive force [15]. This model allows us to describe the spatial dynamics of cells on a crypt–villus geometry and to generate simulated time courses that can be compared to the experimental time courses via time-dependent compartmental models as described below; however, the parameters of the cell-based model cannot be easily inferred from the

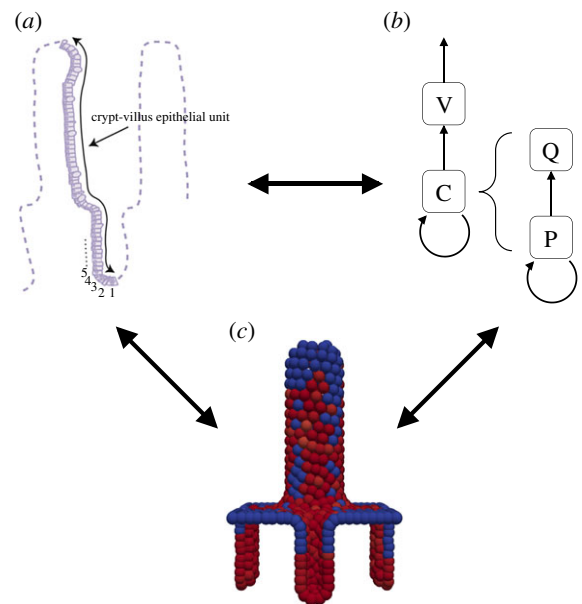


**Figure 1.** Schematic of our approach. (a) Experimental time courses are derived from crypt–villus epithelial units and are analysed by counting labelled cells in the crypt and villus compartments. (b) A compartment-based model accounting for crypt cells (C) and villus cells (V) allows us to quantify cell migration under injury and control. A model extension which distinguishes between a proliferative (P) and a non-proliferative (Q) compartment generates predictions on the dynamics of the number of proliferative and non-proliferative cells in the crypt. (c) A multi-cellular model allows for replication of the experiment and for generation of simulated data; in red and blue are presented labelled and unlabelled cells, respectively. The arrows are interpreted as follows: (a)  $\rightarrow$  (b) (experimental data informing model parametrization): the experimental data allow for inference of the compartment-based model parameters; (b)  $\rightarrow$  (a) (model prediction): the posterior predictive distributions highlight a decrease in the accumulation of labelled cells on villi which is specific of the type of injury (acute or chronic); (a)  $\rightarrow$  (c) (experimental background informing model development): the injuries caused by acute elevated  $\text{TNF}\alpha$  (death and detachment of cells from villus tips) and chronic elevated  $\text{TNF}\alpha$  (less severe, but more persistent, rates of cell death) inform the replication of the experiments (simulated injuries) by means of cell-based simulations and allow for generation of simulated time courses; (b)  $\leftrightarrow$  (c) (consensus between models): the posterior predictive distributions obtained when fitting the compartment based models to data simulated by means of the cell-based model highlight a qualitative agreement with the fits to the experimental data; (c)  $\rightarrow$  (a) (model prediction): the consensus between the models supports the driving role of the injuries caused by acute and chronic elevated  $\text{TNF}\alpha$  in generating treatment-specific decrease in the accumulation of labelled cells on villi.

experimental data since fitting such a detailed and stochastic model would be computationally intensive. By contrast, the compartmental models are described by a smaller number of parameters, since they do not account for the parameters associated with the crypt–villus geometry, and their simulation is computationally inexpensive. These advantages come at the expense of the biological detail included in the model: it accounts only for the time evolution of the number of cells in the crypt and villus compartments and neglects spatial effects. A schematic of our approach is presented in figure 1. As in Parker *et al.* [2], we first developed a compartmental model that distinguishes two compartments, crypt and villus, and obtained quantitative estimates of parameters describing cell proliferation, migration and

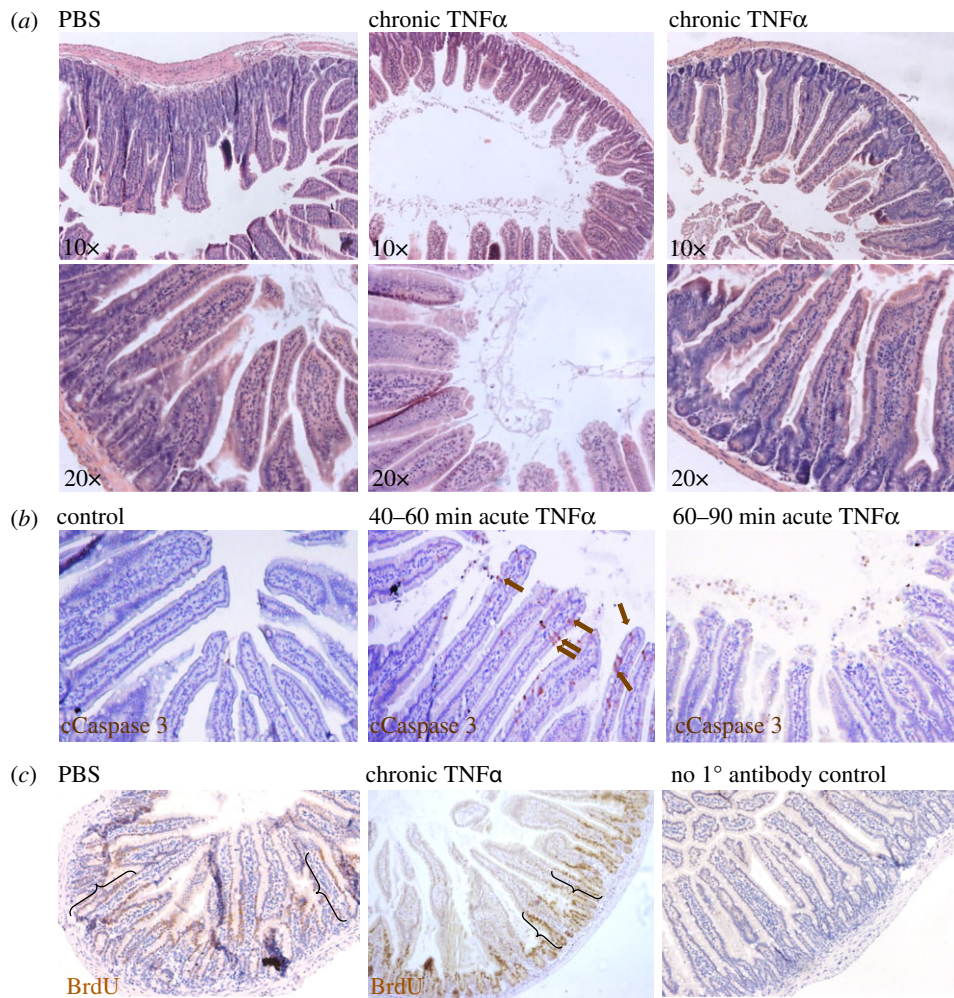


**Figure 2.** Histology and staining of intestinal sections from TNF-treated mice versus controls. (a) H&E staining of small intestinal sections in TNF-treated and control mice. Villus tip damage and cell shedding were observed 60–90 min following acute TNF $\alpha$  treatment (centre panels). Shedding subsided within 2–4 h and by 24 h villus morphology was recovered to near original dimensions. Overt tip shedding was not observed in the chronic setting. (b) Epithelial cell death induced by acute delivery of TNF $\alpha$ . Following single intraperitoneal delivery of TNF $\alpha$ , cleaved-Caspase-3 positive (apoptotic) cells are detectable on villi of proximal small intestine from approximately 40 to 60 mins post-delivery (arrows). (c) BrdU incorporation and migration (example BrdU staining at 24 h shown) was quantified at multiple time points following administration. Brackets for illustration purposes only, position of the labelled front was analysed as labelled cells by position (cell number) from crypt bottom in a continuous strip of epithelial cells from crypt to villus. The labelled cell distribution along the crypt–villus axis was counted for 30–50 individual crypt–villus units per time point, per region, per mouse and analysed as described in the text.

death by fitting it to the experimental data using a variant of Hamiltonian Monte Carlo (the No-U-Turn sampler) [26]. The posterior predictive distributions, showing the simulated time evolution of the number of labelled cells in the crypts and in the villi, produced fits that are in good agreement with the trend of the experimental time courses and highlighted that chronic elevated TNF $\alpha$  caused an increase in cell death, which, in turn, generated a decrease in the accumulation of labelled cells on villi. By contrast, acute elevated TNF $\alpha$  generated a similar, but small, delay. The two-compartment model relies on the simplifying assumption that all cells in the crypts proliferate, whereas in practice only some of them do. For this purpose, we extended the two-compartment model by including a further compartment which enables us to distinguish between proliferative and non-proliferative crypt cells. As for the two-compartment model, the three-compartment model produced fits that are in good agreement with the experimental time courses; in addition, it generated predictions about the dynamics of the number of proliferative and non-proliferative cells in the crypt. To investigate how an increase in cell death may influence an accumulation of labelled cells from the crypt to the

villus, we then used the cell-based model to simulate injury due to treatments causing acute and chronic epithelial cell death. Quantitative estimates of the parameters of the compartmental models, derived by model fitting against these synthetic time courses, revealed a decrease in the accumulation of labelled cells on villi under chronic injury and a minor decrease under acute injury, as experimentally observed. A limit of analysing crypt–villus epithelial units is that it does not address the competition between the progeny of distinct crypt stem cell populations. However, our cell-based simulations account for multiple crypts and they qualitatively agree with the compartmental models describing an average crypt–villus unit, when comparing injuries against controls. This agreement and the increase in the number of parameters in compartmental models accounting for multiple crypts and villi making their parameter values poorly identifiable (e.g. [27]) supports our simplification of analysing average crypt–villus units. The consensus between the compartmental and cell-based models also suggests that injuries caused by acute and chronic elevated TNF $\alpha$  manifest themselves via treatment-specific decreases in the accumulation of labelled cells on villi.

## 2. Methods

### 2.1. Experimental data

#### 2.1.1. Animals

All animal experiments were conducted in strict accordance with the Home Office Animals (Scientific Procedures) Act 1986. Female C57BL/6 mice, aged 10–12 weeks and weighing at least 20 g prior to use in experiments, were housed and maintained in SPF conditions at the University of East Anglia, Norwich, UK in accordance with Home Office regulations, and all procedures were performed by fully trained and licenced researchers. Experimental animals were closely monitored and were sacrificed by rising CO<sub>2</sub> and cervical dislocation, at the timepoints described in the text, prior to subsequent tissue collection. All animals were regularly monitored for clinical signs; any displaying signs beyond those expected within the moderate limits of the procedures would be immediately sacrificed by the above methods and not included in experimental data.

#### 2.1.2. Induction of enterocyte death, cell labelling and tissue processing

Transient, acute elevated circulating TNF $\alpha$  was induced by single intraperitoneal injection of recombinant murine TNF $\alpha$  (Peprotech, London, UK) at 0.5 mg kg<sup>-1</sup>. Chronic elevated circulating TNF $\alpha$  was achieved by hydrodynamic tail vein delivery of TNF $\alpha$ -expressing plasmid (originally a kind gift from C. Gunther, Erlangen, Germany). TNF $\alpha$  overexpression was confirmed by specific ELISA (Thermo Fisher Scientific, Waltham, USA) for elevated levels in blood plasma over a minimum of 14 days, and in liver and intestinal tissue lysates post mortem. The thymine analogue 5-bromo-2-deoxyuridine, BrdU (Sigma-Aldrich, Paisley, UK) was administered at 50 mg kg<sup>-1</sup> body weight by single intraperitoneal injection. In the case of acute elevated TNF $\alpha$ , BrdU was delivered simultaneously with TNF $\alpha$ . In the chronic TNF experiments, BrdU time courses were performed once elevated blood TNF $\alpha$  levels had been established. At time points from 1 h to 48 h post-BrdU administration, mice were euthanized and intestinal tracts were removed, dissected, formalin-fixed and paraffin embedded. Transverse sections of duodenum and ileum were prepared at 5  $\mu$ m and were immunostained for BrdU using biotinylated anti-BrdU antibody (AbCam, Cambridge, UK), Neutravidin-HRP (Thermo Fisher), and diaminobenzidine reaction (DAB, Dako, Glostrup, Denmark). Villus cell shedding was confirmed histologically by Caspase-3 (anti-CC3, R&D Systems, Minneapolis, USA) labelling of apoptotic cells in FFPE duodenal and ileal sections counterstained with H&E.

#### 2.1.3. Data collection

Collection of the experimental dataset followed the format described in Parker *et al.* [2]. Although many crypts contribute to a single villus, our experimental data and analysis describe single crypt–villus epithelial units, i.e. a single continuous strip of epithelial cells running from the base of a particular crypt to the tip of the associated villus, all within the same single strip of contiguous epithelial cells. The number of unlabelled and BrdU-labelled cells by position, from crypt base to neighbouring villus tip, was counted for 30–50 individual crypt–villus units per section, per region, per mouse to provide a good estimate of the average behaviour of any individual strip *in vivo* (average crypt–villus epithelial units). Counts were recorded as binary values; this generated, for each replicate and at each time point, a binary vector whose length varied with the particular sample. Counts were taken at multiple time points post-delivery of BrdU and post delivery of TNF $\alpha$  (histology and staining of intestinal sections from

TNF-treated mice versus controls are shown in figure 2). The counts and the code to calculate the experimental time courses are reported in the electronic supplementary material (folder Counts at <https://tinyurl.com/y9xk3nsk>). The number of samples for each time point are shown in electronic supplementary material, tables S1 and S2. The boundary between the crypt and villus compartment was estimated from all datasets obtained during the first 2 h after BrdU injection as the cell position closest to the crypt bottom and such that the fraction of labelled cells in the villus is smaller than 0.01. The time courses obtained from the ileum are presented in figure 3*a*; the corresponding time courses from the duodenum are presented in figure 3*b*.

### 2.2. Compartment-based models

To analyse the spatio-temporal dynamics of BrdU-labelled cells, we derived two compartmental models formulated as a system of time-dependent ODEs. The first model treats the crypt–villus unit as two distinct compartments and distinguishes the cell numbers in the crypt and villus; the second model decomposes the crypt–villus unit into three compartments and distinguishes between proliferative and non-proliferative cells in the crypt. For simplicity, and to allow for parameter estimation, in what follows we model labelled cells only.

#### 2.2.1. Two-compartment model

We distinguish two cellular compartments: labelled cells in the crypt, whose number at time  $t$  is denoted by  $C = C(t)$ ; and labelled cells in the villus, whose number is denoted by  $V = V(t)$ . We introduce two parameter thresholds  $C^*$ ,  $V^*$  such that when  $C(t) > C^*$  labelled cells in the crypt start migrating onto the villus, and when  $V(t) > V^*$  cells begin to be shed from the villus. We denote condition-specific death rates in the crypt and villus compartment as follows:

$$\mu_c^{(\text{condition})} = \begin{cases} 0 & \text{in control (BrdU)} \\ \mu_{c_a} & \text{during acute injury} \\ \mu_{c_c} & \text{during chronic injury} \end{cases} \quad (2.1)$$

$$\mu_v^{(\text{condition})} = \begin{cases} 0 & \text{in control (BrdU)} \\ \mu_{v_a} & \text{during acute injury} \\ \mu_{v_c} & \text{during chronic injury} \end{cases}$$

where  $\mu_{c_a}$ ,  $\mu_{c_c}$ ,  $\mu_{v_a}$  and  $\mu_{v_c}$  are positive constants. Defining by

$$H(x) = \begin{cases} 0 & \text{if } x < 0 \\ 1 & \text{if } x \geq 0 \end{cases}$$

the Heaviside function, the two-compartment model is described by the following pair of ODEs:

$$\left. \begin{aligned} \frac{dC}{dt} &= \lambda C - \gamma(C - C^*)H(C - C^*) - \mu_c^{(\text{condition})}C \\ \text{and } \frac{dV}{dt} &= \gamma(C - C^*)H(C - C^*) - \gamma_s(V - V^*)H(V - V^*) - \mu_v^{(\text{condition})}V \end{aligned} \right\} \quad (2.2)$$

where  $\lambda$  is the net cell proliferation rate (cell proliferation minus cell death rate),  $\gamma$  is the cell migration rate between the two compartments,  $\gamma_s$  is the cell shedding rate from the villus. Model parameters and initial conditions, included in the set of parameters to be estimated, are listed in table 1.

#### 2.2.2. Three-compartment model

The three-compartment model subdivides the crypt into proliferative and non-proliferative cells and defines the following compartments: labelled proliferative cells in the crypt, whose number at time  $t$  is denoted by  $P = P(t)$ ; labelled non-proliferative cells in the crypt, whose number is denoted by  $Q = Q(t)$ ; and labelled non-proliferative cells on the villus, whose number is

**Table 1.** Summary of the parameters and initial conditions that appear in the two-compartment model defined by equations (2.2).

parameter	description	units
$\lambda$	proliferation rate	$\text{h}^{-1}$
$\gamma$	migration rate into the villus	$\text{h}^{-1}$
$\mu_c$	death rate in the crypt during acute injury	$\text{h}^{-1}$
$\mu_v$	death rate in the villus during acute injury	$\text{h}^{-1}$
$\mu_c$	death rate in the crypt during chronic injury	$\text{h}^{-1}$
$\mu_v$	death rate in the villus during chronic injury	$\text{h}^{-1}$
$C^*$	number of labelled cells in the crypt above which migration to the villus starts	—
$C_0 \equiv C(t=0)$	initial number of labelled cells in crypt	—
$V_0 \equiv V(t=0)$	initial number of labelled cells on villus	—

denoted by  $V = V(t)$  (cells on the villus do not proliferate). For comparison with the two compartment model, we also denote by  $C(t) = P(t) + Q(t)$  the total number of labelled cells in the crypt. We introduce three parameter thresholds  $P^*$ ,  $Q^*$ ,  $V^*$  such that when  $P(t) > P^*$  labelled proliferative cells start migrating onto the villus, when  $Q(t) > Q^*$  non-proliferative labelled cells start migrating onto the villus and when  $V(t) > V^*$  cell shedding begins to occur from the villus. As we set up the crypt–villus boundary at the cell position closest to the crypt bottom where we detected proliferative cells, we deemed both proliferative and non-proliferative cells as likely to pass this threshold and to be transferred to the non-proliferative villus compartment. Alternatively, other boundaries (such as the crypt mouth) between crypt and villus could be considered. Depending on where the boundary is located one could argue that only non-proliferative cells are transferred onto the villus or that the rates of transfer are not equal for proliferative and non-proliferative cells. In what follows, we assume that both proliferative and non-proliferative cells can migrate onto villi and may be affected by acute and chronic injury; for simplicity, we assume equal rates of cell transfer onto villi and of cell death in the crypts. We denote condition-specific death rates in the crypt and villus compartments as for the two-compartment model (see equations (2.1)). The three-compartment model is described by the following system of time-dependent ODEs:

$$\text{and } \left. \begin{aligned} \frac{dP}{dt} &= (\lambda - \gamma_c)P - \gamma_v(P - P^*)H(P - P^*) - \mu_c^{(\text{condition})}P, \\ \frac{dQ}{dt} &= \gamma_cP - \gamma_v(Q - Q^*)H(Q - Q^*) - \mu_c^{(\text{condition})}Q \\ \frac{dV}{dt} &= \gamma_v(P - P^*)H(P - P^*) + \gamma_v(Q - Q^*)H(Q - Q^*) \\ &\quad - \gamma_s(V - V^*)H(V - V^*) - \mu_v^{(\text{condition})}V, \end{aligned} \right\} \quad (2.3)$$

where  $\lambda$  is the cell net proliferation rate,  $\gamma_c$  is the rate at which cells differentiate from a proliferative to a non-proliferative state,  $\gamma_v$  is the rate at which cells migrate onto the villus,  $\gamma_s$  is the rate of cell shedding from the villus and  $H$  is the Heaviside function. Model parameters and initial conditions, included in the set of parameters to be estimated, are listed in table 2.

### 2.3. Cell-based simulations

We simulated injury by using a cell-based simulation of cell dynamics on a patch of intestinal epithelium composed of multiple crypts and a single villus, previously developed by Mirams *et al.* [15], and generated synthetic time courses.

The model is a stochastic three-dimensional off-lattice cell centre-based model confined to a two-dimensional surface

comprising four crypts that surround a single villus; the crypts and the villus are modelled using a cylindrical geometry with spherical rims. Cell movement is driven by a nearest-neighbour-defined force, previously employed by Meineke *et al.* [9]. Each pair of neighbouring nodes is assumed to be connected by a linear spring. The force of node  $i$  is given by

$$\mathbf{F}_i(t) = \sum_j \mu_{i,j} (\|\mathbf{r}_{ij}\| - s_{i,j}(t)) \hat{\mathbf{r}}_{ij},$$

where  $\mu_{i,j}$  is the spring constant for the spring between nodes  $i$  and  $j$ ,  $s_{i,j}(t)$  is its natural length at time  $t$ ,  $\mathbf{r}_{i,j}$  is their relative displacement and a hat ( $\hat{\cdot}$ ) denotes a unit vector. Cells moving above a plane defined at the villus tip are removed due to anoikis. Injury is simulated either by removing cells randomly (during chronic injury) or by initially removing cells that are above a plane defined at two-thirds of the villus height (to account for the experimentally observed detachment of cells at the top third of the villus during acute injury). Cell proliferation depends on a decreasing gradient of the Wnt family of morphogens from the crypt to the villus [28], and it is modelled by defining a linear gradient in Wnt concentration up the crypt, allowing cells to divide when their Wnt concentration exceeds a fixed threshold (see SimpleWntCellCycleModel class for details [15]).

All simulations were initialized without including any random removal of cells and were run for 1000 h with default parameter values [15], at which time the total number of cells in the crypts and in the villus was approximately constant. After initialization, cell-based simulations at homeostasis (control) were run for 80 h with default parameter values. During this time period, crypt cells were labelled and their lineage was tracked according to their ancestor proliferative cell. Acute injury was modelled by initially detaching cells from the top third of the villus. Regeneration of this area, due to cell migration from the crypts, was simulated for 80 h. Chronic injury was introduced by randomly killing cells in the crypts and the villus with the default probability value  $p = 0.005 \text{ h}^{-1}$ .

### 2.4. Parameter estimation

The compartmental models were solved using the R packages deSolve (Classical Runge–Kutta 4th-Order Integration) [29] and RSTAN [26]. STAN is a C++ library that performs Bayesian inferences using the No-U-Turn sampler (a variant of Hamiltonian Monte Carlo); the RSTAN package conveniently allows STAN to be used from R. RSTAN was applied to equations (2.2) and (2.3) with uniform priors represented in electronic supplementary material, figures S13, S15, S17, S19, S21 and S23. Convergence diagnostics were then calculated for four Markov chain Monte Carlo (MCMC) chains using the R package CODA, which provides routines for output analysis and

**Table 2.** Summary of the parameters and initial conditions that appear in the three-compartment model defined by equations (2.3).

parameter	description	units
$\lambda$	proliferation rate	$\text{h}^{-1}$
$\gamma_c$	migration rate from proliferative to non-proliferative state	$\text{h}^{-1}$
$\gamma_v$	migration rate into the villus	$\text{h}^{-1}$
$\gamma_s$	cell shedding rate	$\text{h}^{-1}$
$\mu_c$	death rate in the crypt during acute injury	$\text{h}^{-1}$
$\mu_v$	death rate in the villus during acute injury	$\text{h}^{-1}$
$\mu_c$	death rate in the crypt during chronic injury	$\text{h}^{-1}$
$\mu_v$	death rate in the villus during chronic injury	$\text{h}^{-1}$
$P^*$	number of proliferative and labelled cells in the crypt above which migration to non-proliferative state starts	—
$Q^*$	number of non-proliferative and labelled cells in the crypt above which migration to the villus starts	—
$V^*$	number of labelled cells in the villus above which cell shedding starts	—
$P_0 \equiv P(t=0)$	initial number of labelled proliferative cells in crypt	—
$Q_0 \equiv Q(t=0)$	initial number of labelled non-proliferative cells in crypt	—
$V_0 \equiv V(t=0)$	number of labelled cells in villus (all non-proliferative)	—

diagnostics for MCMC [30]. Where multi-modality was highlighted by chains mixing around different modes, the chains with the highest fit quality (STAN log probability variable  $\text{lp}_\_$ ) were selected. The initial conditions for  $P(t)$ ,  $Q(t)$  (three-compartment model) and  $C(t)$  (two-compartment model) were included in the set of parameters to be estimated by applying MCMC. Since the number of labelled cells in the villus ( $V(t)$ ) is approximately zero at the start of the time courses, we assumed that migration of labelled cells onto villi may be initially neglected.

### 3. Results

In what follows, we first describe the predictions of our compartmental and cell-based models regarding the influence of elevated  $\text{TNF}\alpha$  on epithelial homeostasis; we then discuss the parameters inferred when fitting the compartmental models to experimental and simulated data.

#### 3.1. Accumulation of labelled cells on villi is delayed during chronic epithelial damage

The two- and three-compartment models were fitted against the experimental data derived from the ileum and the duodenum as described in the Methods section. The resulting posterior predictive distributions are shown in figures 4 and 5 and electronic supplementary material, figures S2 and S3. Both models reproduce the trend of the experimental data and show a delay in migration during chronic injury compared to control (figure 6 and electronic supplementary material, figure S4). Acute epithelial damage causes a modest delay in cell migration terms in the ileum and a very small decrease in the duodenum (figure 6 and electronic supplementary material, figure S4). These findings may appear counterintuitive, since some inflammatory conditions are associated with crypt enlargement. However, we did not observe epithelial hyperproliferation or increased crypt size in our  $\text{TNF}$ -driven damage model. In fact, the number of crypt cells was slightly reduced, likely due to increased cell death during damage.

The parameter posterior distributions obtained in the duodenum compared to the ileum highlight higher cell proliferation rates (see electronic supplementary material, figures S8 and S9) leading to higher values of the migration terms (figure 6 and electronic supplementary material, figure S4). Although it is currently unknown why the proliferation rates are differing in the duodenum, they likely reflect local stem cell responses to the differencing microbial, immunological and metabolic cues.

#### 3.2. Cell-based simulations suggest that injuries drive treatment-specific delays in cell migration

The cell-based model was simulated as described in §2.3. Typical simulation results are presented in the electronic supplementary material (file *Cell\_Based\_Simulations.pptx* at <https://tinyurl.com/y9xk3nsk>). Electronic supplementary material, figure S1, shows the mean and standard errors of simulated time series of labelled cells generated by ten simulations for each condition. Compared to control simulations, the simulated persistent, increased rate of cell death associated with chronic injury appears to hinder the migration of labelled crypt cells onto the villus. Conversely, the initial detachment of cells from the villus tip caused by simulated acute injury does not seem to affect significantly cell migration from the crypts to the villus and the villus tip regenerates due to cell migration from the crypts. To confirm these effects, we then fitted the compartmental models to the time courses generated from simulations of the cell-based model. The simulated data were fitted up to 50 h to emulate the duration of the experimental time courses. Electronic supplementary material, figures S5 and S6, show the posterior predictive distributions of the two- and three-compartment models together with the predicted migration terms. As observed when applying the model to the experimental data, an increase in cell death caused a delay in the accumulation of labelled cells on villi during simulated chronic injury and a minor delay due to simulated acute injury (electronic supplementary material, figure S7). The posterior distributions of the parameter are presented in

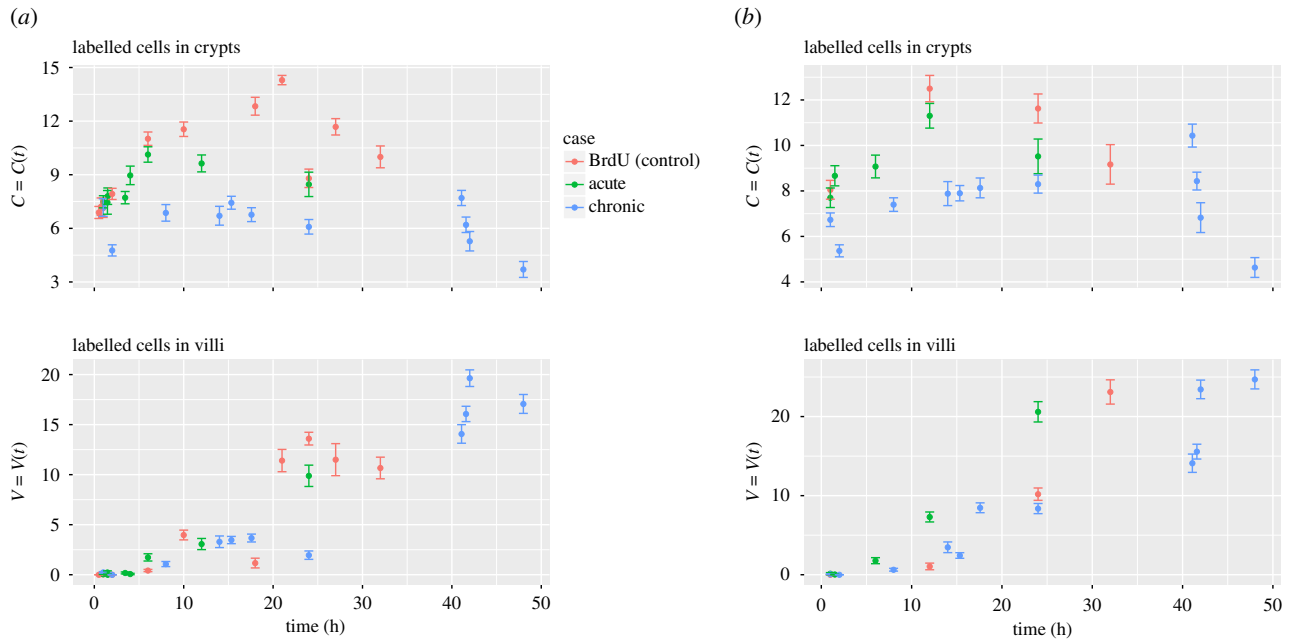


**Figure 3.** Experimental data. Time series representing average numbers of cells in crypts  $C = C(t)$  and villi  $V = V(t)$  during acute injury, chronic injury and control (BrdU) in ileum (a) and duodenum (b). Error bars indicate standard errors.

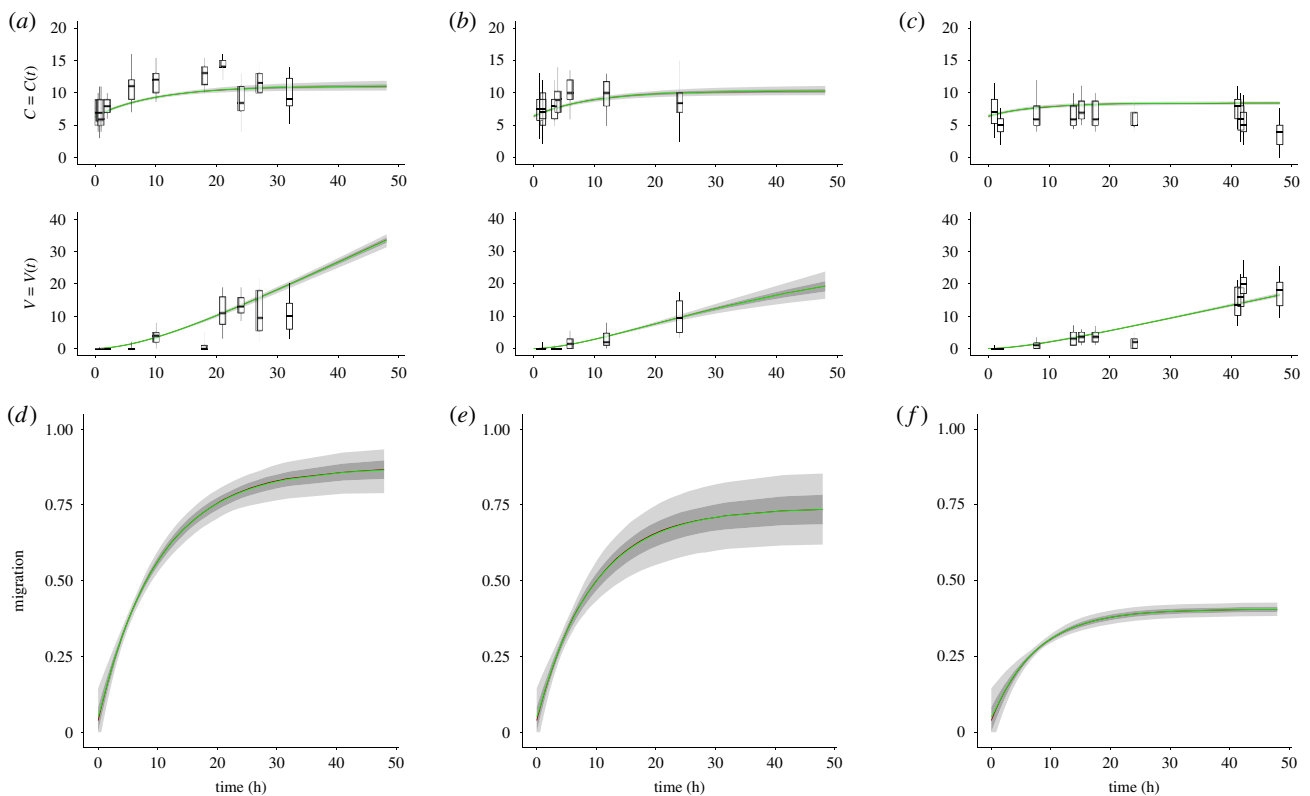


**Figure 4.** Fits of the two-compartment model to ileal time course data. (a–c) Posterior predictive distributions and estimates of parameter uncertainty obtained by fitting the two-compartment model (equations (2.1)) against ileal time courses. Posterior predictive distributions inferred from (a) BrdU (control), (b) acute injury, (c) chronic injury experimental time courses. Boxplots represent the 0.05, 0.25, 0.75, 0.95 quantiles of the experimental data. Dark and light grey area plots represent the [0.25, 0.75] and the [0.05, 0.95] quantiles of the posterior predictive distributions, respectively. The green line indicates the posterior mean; the red line, partially overlapping the green line, represents the posterior median. (d–f) Plots representing the posterior predictive distribution of the migration term  $\gamma(C - C^*)H(C - C^*)$  in the ileum obtained from control (BrdU) (d), acute injury (e) and chronic injury (f) time courses. The contribution to migration is reduced during chronic injury.

electronic supplementary material, figures S8–S23. A prolonged delay in the accumulation of labelled cells on villi during chronic injury compared to acute injury is caused by the combined increase in the death rates in the crypts ( $\mu_c$ ) and in the villi ( $\mu_v$ ), (electronic supplementary material,

figures S8–S11). We finally analysed the influence of the geometry of the set-up chosen for the cell-based simulations on the migration terms by simulating time courses when varying crypt and villus lengths and radii. These time courses were fitted using the two-compartment model and the migration

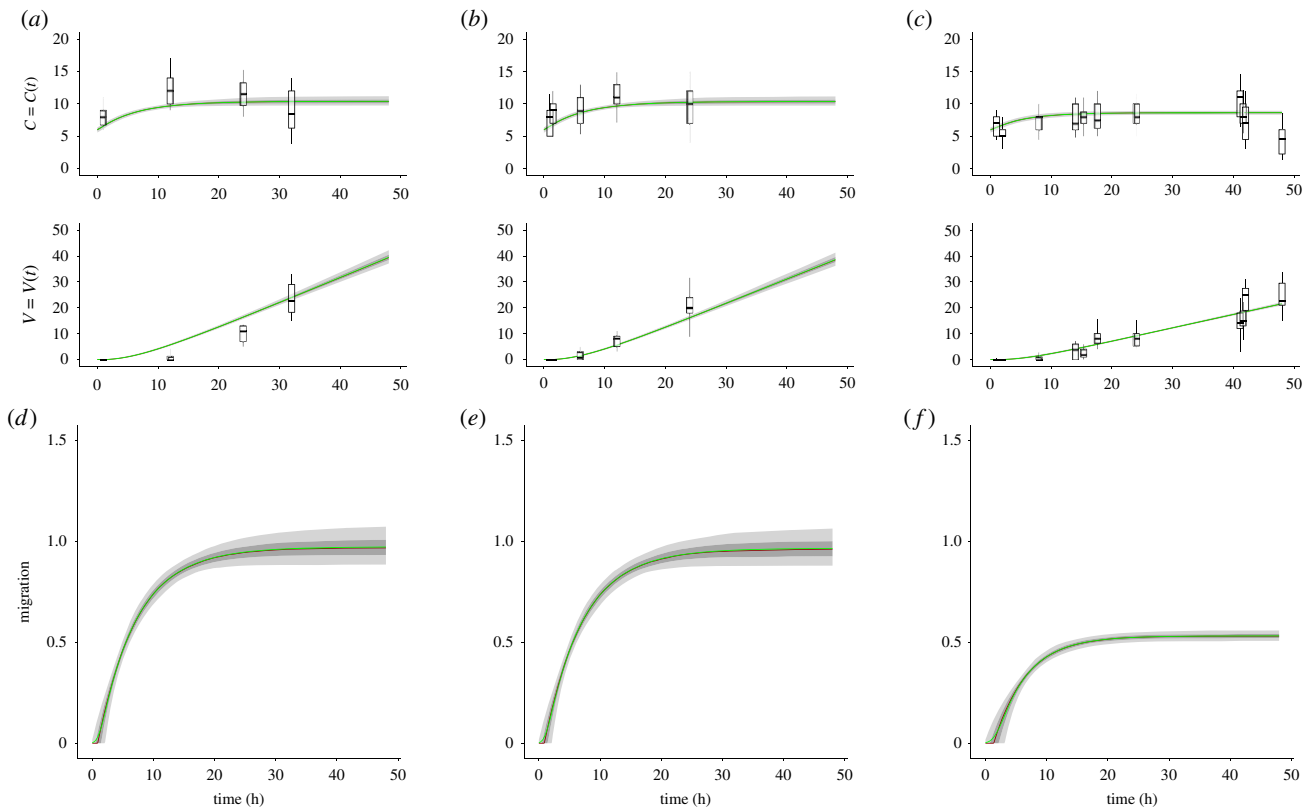


**Figure 5.** Fits of the two-compartment model to duodenal time course data. (a–c) Posterior predictive distributions and estimates of parameter uncertainty obtained by fitting the two-compartment model (equations (2.1)) against duodenal time courses. Posterior predictive distributions inferred from (a) BrdU (control), (b) acute injury, (c) chronic injury experimental time courses. Boxplots represent the 0.05, 0.25, 0.75, 0.95 quantiles of the experimental data. Dark and light grey area plots represent the [0.25, 0.75] and the [0.05, 0.95] quantiles of the posterior predictive distributions, respectively. The green line indicates the posterior mean; the red line, partially overlapping the green line, represents the posterior median. (d–f) Plots representing the posterior predictive distribution of the migration term  $\gamma(C - C^*)H(C - C^*)$  in the duodenum obtained from control (BrdU) (d), acute injury (e) and chronic injury (f) time courses. The contribution to migration is reduced during chronic injury.

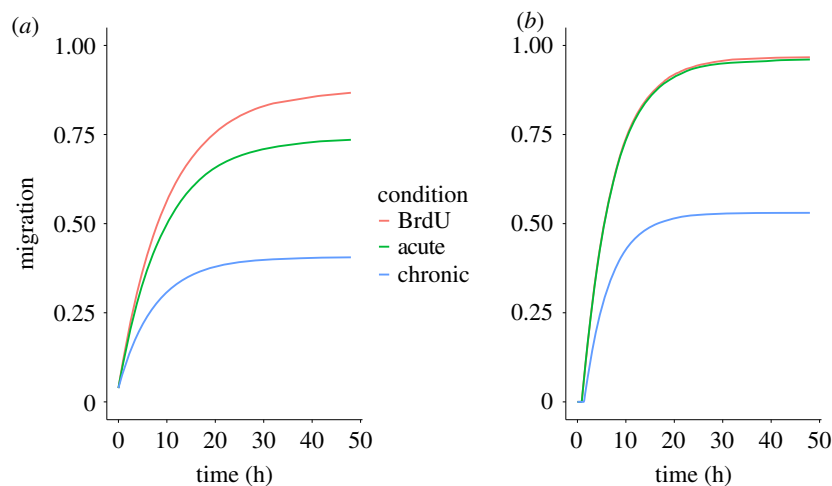


**Figure 6.** Migration terms of the two-compartment model when fitted against experimental time courses. Plots representing the medians of the posterior predictive distribution of the migration terms  $\gamma(C - C^*)H(C - C^*)$  in ileum (a) and in duodenum (b). Contribution to migration is reduced during simulated chronic injury.

terms were derived from the fitted model. The results are discussed in the section ‘Influence of the geometry of the set-up chosen for the cell-based simulations on the migration terms’ in the electronic supplementary material. Whereas an increase in villus length or radius plays a minor role in the migration term, an increase in crypt length or radius causes faster cell migration onto the villus (see electronic supplementary material, figures S32–S34).

### 3.3. Small regions of the parameter search space allow for good-quality fits

Highly correlated parameters may be found in both of the compartment models. In particular, the pairs  $(\lambda, \mu_c)$  and  $(\gamma, C^*)$  are the most strongly correlated parameters in the two-compartment model in both tissues (electronic supplementary material, figures S12 and S14); whereas,  $(\lambda, \gamma_c)$ ,

$(\lambda, P^*), (\gamma_c, P^*), (\lambda, P_0), (P^*, P^0), (P_0, Q_0)$  are the most correlated pairs in the three-compartment model in both tissues (electronic supplementary material, figures S16 and S18). Highly correlated pairs were also found when fitting the compartment models against simulated data; for example,  $(\lambda, C_0), (\gamma, C^*), (\lambda, \gamma_s)$  in the two-compartment model (electronic supplementary material, figure S20) and  $(\lambda, \gamma_c), (\lambda, P^*), (\gamma_c, P^*), (\lambda, P_0), (P^*, P^0), (P_0, Q_0)$  and others in the three-compartment model (electronic supplementary material, figure S22). Notwithstanding this dependence between different parameters, density plots of the posterior distributions highlight that relatively small regions of the parameter search space, defined by uniform prior distributions, allow for good-quality fits (electronic supplementary material, figures S13, S15, S17, S19, S21 and S23).

### 3.4. The time thresholds associated with cell migration and cell shedding are most sensitive to crypt parameters

Because of the increase of the death rates  $\mu_c$  and  $\mu_v$  during acute and chronic injury, we analysed how changes in these parameters in the two-compartment model may affect the time thresholds above which cell migration and cell shedding begin. More precisely, we denoted by  $t_C^*$  and  $t_V^*$  the time thresholds after which  $C(t) > C^*$  and  $V(t) > V^*$ , respectively. Simulation of the perturbed model highlighted that increasing  $\mu_c$  causes a delay in both time thresholds, whereas  $\mu_v$  only affects  $t_V^*$  (electronic supplementary material, figure S24). Electronic supplementary material, figures S25–S27, show how the time thresholds vary when all model parameters are varied and highlight that both thresholds are most sensitive to  $\lambda$ ,  $\mu_c$  and  $C_0$ . Similar effects were found when simulating the three-compartment model by defining the thresholds  $t_P^*$ ,  $t_Q^*$ ,  $t_C^*$  and  $t_V^*$ , after which  $P(t) > P^*$ ,  $Q(t) > Q^*$ ,  $C(t) := P(t) + Q(t) > P^* + Q^* =: C^*$  and  $V(t) > V^*$ , respectively. Simulation of the perturbed model highlighted that increasing  $\mu_c$  causes all time thresholds ( $t_P^*$ ,  $t_Q^*$ ,  $t_C^*$ ,  $t_V^*$ ) to increase, whereas increasing  $\mu_v$  causes an increase in  $t_V^*$  only (electronic supplementary material, figure S28). Figures S29–S31 in the electronic supplementary material show how the time thresholds vary when all other model parameters vary and highlight that all of these thresholds are extremely sensitive to the values of  $\lambda$ ,  $\mu_c$ ,  $\gamma_c$  and  $P_0$ .

## 4. Discussion

By combining cell tracking methods with computational models, we derived quantitative estimates of the proliferative activity of crypt stem cells and of their influence on villus cell migration during TNF $\alpha$ -driven epithelial injury conditions. Experimental time courses were analysed by fitting the data to compartmental models with two and three compartments. Both fitted models were able to reproduce well the trend of the experimental time courses. The three-

compartment model allowed prediction of the time evolution of proliferative and non-proliferative cells at the expense of requiring estimation of a greater number of unknown parameter values when compared with the two-compartment model. The posterior parameter and predictive distributions highlighted in both models that, whereas an acute and temporary increase in cell death did not influence distinctly net cell proliferation (new born cells minus dead cells) and migration onto the villus, a prolonged and less severe injury caused a decrease in net cell proliferation which produced, in turn, a delayed migration. To further investigate how injury may affect the dynamics of cells in the epithelium and trigger such delay, we simulated cell death, initiated by TNF $\alpha$ , by means of a cell-based model and generated simulated time courses. Analysis of these time courses by means of compartmental models showed delayed migration under simulated chronic injury as experimentally observed, highlighting how a prolonged increase in cell death affects the dynamics of cells in the epithelium by delaying their migration. In summary, integration of computational modelling with experimental data derived from cell-tracking methods allowed us to distinguish which conditions influence epithelial cell dynamics. Identification of such conditions may highlight their contribution to barrier dysfunction in the development of intestinal inflammation. To the best of our knowledge, an experimental and computational analysis of cell dynamics during villus injury such as the one described in this article, which integrates compartmental and cell-based models with novel experimental time courses, has not been presented before. We believe that this analysis may stimulate further experimental work to estimate, for example, the proportion of proliferative and non-proliferative cells in the crypts.

**Ethics.** All animal experiments were conducted in strict accordance with the Home Office Animals (Scientific Procedures) Act 1986.

**Data accessibility.** The datasets supporting this article have been uploaded as part of the electronic supplementary material.

**Authors' contributions.** D.M. and A.A.A. performed the computational analysis of the mathematical models; A.P. and L.V. designed and performed the experiments; S.F. contributed to implementing the inference of the model parameters; A.G.F., P.K.M. and H.M.B. contributed to designing the work and developing the mathematical models; A.J.M.W. participated in designing the work and in experimental planning; C.P. contributed to project design, mathematical model development, experimental planning and data analysis. All of the authors contributed to writing the manuscript.

**Competing interests.** We declare we have no competing interests.

**Funding.** This work was funded by the Biotechnology and Biological Sciences Research Council (BBSRC)-UK projects BB/K018256/1, BB/K017578/1, BB/K017144/1 and BB/J004529/1, by the Engineering and Physical Sciences Research Council (EPSRC)-UK project EP/I017909 and by Cancer Research UK (CRUK) grant no. C5255/A23225, through a Cancer Research UK Oxford Centre Prize DPhil Studentship.

**Acknowledgments.** We thank Hunter Rice and the journal club on computational biology at the Department of Microbiology, University of Tennessee, Knoxville for helpful comments.

## References

1. Watson AJM, Hughes KR. 2012 TNF $\alpha$ -induced intestinal epithelial cell shedding: implications for intestinal barrier function. *Ann. NY Acad. Sci.* **1258**, 1–8. (doi:10.1111/j.1749-6632.2012.06523.x)
2. Parker A, Maclaren OJ, Fletcher AG, Muraro D, Kreuzaler PA, Byrne HM, Maini PK, Watson AJM,

- Pin C. 2016 Cell proliferation within small intestinal crypts is the principal driving force for cell migration on villi. *FASEB J.* **31**, 636–649. (doi:10.1096/fj.201601002)
3. Becker C, Watson AJ, Neurath MF. 2013 Complex roles of caspases in the pathogenesis of inflammatory bowel disease. *Gastroenterology* **144**, 283–293. (doi:10.1053/j.gastro.2012.11.035)
  4. Britton NF, Wright NA, Murray JD. 1982 A mathematical model for cell population kinetics in the intestine. *J. Theor. Biol.* **98**, 531–541. (doi:10.1016/0022-5193(82)90135-7)
  5. Johnston MD, Edwards CM, Bodmer WF, Maini PK, Chapman SJ. 2007 Mathematical modeling of cell population dynamics in the colonic crypt and in colorectal cancer. *Proc. Natl Acad. Sci. USA* **104**, 4008–4013. (doi:10.1073/pnas.0611179104)
  6. Murray PJ, Walter A, Fletcher AG, Edwards CM, Tindall MJ, Maini PK. 2011 Comparing a discrete and continuum model of the intestinal crypt. *Phys. Biol.* **8**, 26011. (doi:10.1088/1478-3975/8/2/026011)
  7. Loeffler M, Stein R, Wichmann H-E, Potten CS, Kaur P, Chwalinski S. 1986 Intestinal cell proliferation. I. A comprehensive model of steady-state proliferation in the crypt. *Cell Prolif.* **19**, 627–645. (doi:10.1111/j.1365-2184.1986.tb00763.x)
  8. Loeffler M, Potten CS, Paulus U, Glatzer J, Chwalinski S. 1988 Intestinal crypt proliferation. II. Computer modelling of mitotic index data provides further evidence for lateral and vertical cell migration in the absence of mitotic activity. *Cell Prolif.* **21**, 247–258. (doi:10.1111/j.1365-2184.1988.tb00784.x)
  9. Meineke FA, Potten CS, Loeffler M. 2001 Cell migration and organization in the intestinal crypt using a lattice-free model. *Cell Prolif.* **34**, 253–266. (doi:10.1046/j.0960-7722.2001.00216.x)
  10. van Leeuwen IMM *et al.* 2009 An integrative computational model for intestinal tissue renewal. *Cell Prolif.* **42**, 617–636. (doi:10.1111/j.1365-2184.2009.00627.x)
  11. Mirams GR, Fletcher AG, Maini PK, Byrne HM. 2012 A theoretical investigation of the effect of proliferation and adhesion on monoclonal conversion in the colonic crypt. *J. Theor. Biol.* **312**, 143–156. (doi:10.1016/j.jtbi.2012.08.002)
  12. Buske P, Galle J, Barker N, Aust G, Clevers H, Loeffler M. 2011 A comprehensive model of the spatio-temporal stem cell and tissue organisation in the intestinal crypt. *PLoS. Comput. Biol.* **7**, e1001045. (doi:10.1371/journal.pcbi.1001045)
  13. Pin C, Watson AJM, Carding SR. 2012 Modelling the spatio-temporal cell dynamics reveals novel insights on cell differentiation and proliferation in the small intestinal crypt. *PLoS ONE* **7**, e37115. (doi:10.1371/journal.pone.0037115)
  14. Dunn S-J, Näthke IS, Osborne JM. 2013 Computational models reveal a passive mechanism for cell migration in the crypt. *PLoS ONE* **8**, e80516. (doi:10.1371/journal.pone.0080516)
  15. Mirams GR *et al.* 2013 Chaste: an open source C++ library for computational physiology and biology. *PLoS Comput. Biol.* **9**, e1002970. (doi:10.1371/journal.pcbi.1002970)
  16. Ingham-Dempster T, Walker DC, Corfe BM. 2017 An agent-based model of anoikis in the colon crypt displays novel emergent behaviour consistent with biological observations. *R. Soc. open. sci.* **4**, 160858. (doi:10.1098/rsos.160858)
  17. Ingham-Dempster T, Corfe B, Walker D. 2017 A cellular based model of the colon crypt suggests novel effects for Apc phenotype in colorectal carcinogenesis. *J. Comput. Sci.* **24**, 125–131. (doi:10.1016/j.jocs.2017.06.013)
  18. Maclaren OJ, Parker A, Pin C, Carding SR, Watson AJM, Fletcher AG, Byrne HM, Maini PK. 2017 A hierarchical Bayesian model for understanding the spatiotemporal dynamics of the intestinal epithelium. *PLoS. Comput. Biol.* **13**, e1005688. (doi:10.1371/journal.pcbi.1005688)
  19. Kontoyiannis D, Pasparakis M, Pizarro TT, Cominelli F, Kollias G. 1999 Impaired on/off regulation of TNF biosynthesis in mice lacking TNF AU-rich elements: implications for joint and gut-associated immunopathologies. *Immunity* **10**, 387–398. (doi:10.1016/S1074-7613(00)80038-2)
  20. Armaka M, Apostolaki M, Jacques P, Kontoyiannis DL, Elewaut D, Kollias G. 2008 Mesenchymal cell targeting by TNF as a common pathogenic principle in chronic inflammatory joint and intestinal diseases. *J. Exp. Med.* **205**, 331–337. (doi:10.1084/jem.20070906)
  21. Roulis M, Armaka M, Manoloukos M, Apostolaki M, Kollias G. 2011 Intestinal epithelial cells as producers but not targets of chronic TNF suffice to cause murine Crohn-like pathology. *Proc. Natl Acad. Sci. USA* **108**, 5396–5401. (doi:10.1073/pnas.1007811108)
  22. Lau KS, Cortez-Retamozo V, Philips SR, Pittet MJ, Lauffenburger DA, Haigis KM. 2012 Multi-scale in vivo systems analysis reveals the influence of immune cells on TNF- $\alpha$ -induced apoptosis in the intestinal epithelium. *PLoS Biol.* **10**, e1001393. (doi:10.1371/journal.pbio.1001393)
  23. Williams JM *et al.* 2013 A mouse model of pathological small intestinal epithelial cell apoptosis and shedding induced by systemic administration of lipopolysaccharide. *Dis. Model. Mech.* **6**, 1388–1399. (doi:10.1242/dmm.013284)
  24. Schaubek M *et al.* 2016 Dysbiotic gut microbiota causes transmissible Crohn's disease-like ileitis independent of failure in antimicrobial defence. *Gut* **65**, 225–237. (doi:10.1136/gutjnl-2015-309333)
  25. Wright NA, Irwin M. 1982 The kinetics of villus cell populations in the mouse small intestine. I. Normal villi: the steady state requirement. *Cell Tissue Kinet.* **15**, 595–609. (doi:10.1111/j.1365-2184.1982.tb01066.x)
  26. The Stan Development Team. 2017 Stan Modeling Language User's Guide and Reference Manual. See <http://mc-stan.org>.
  27. Barthel ER. 2017 On the utility of a compartmental population kinetics model of intestinal epithelial stem cell proliferation and differentiation. *Theor. Biol. Med. Model.* **14**, 25. (doi:10.1186/s12976-017-0071-8)
  28. Gaspar C, Fodde R. 2004 APC dosage effects in tumorigenesis and stem cell differentiation. *Int. J. Dev. Biol.* **48**, 377–386. (doi:10.1387/ijdb.041807cg)
  29. Soetaert K, Petzoldt T, Setzer RW. 2010 Solving differential equations in R: package deSolve. *J. Stat. Softw.* **33**, 1–25. (doi:10.18637/jss.v033.i09)
  30. Plummer M, Best N, Cowles K, Vines K. 2006 CODA: convergence diagnosis and output analysis for MCMC. *R News* **6**, 7–11.